PAPER

Sub-mm³ dimensional scaling of fully-integrated additively-fabricated microsupercapacitors for embedded energy storage applications†

Amin Hodaei [ID] [a] and Vivek Subramanian*[ab]

Microsupercapacitors (MSCs) are attractive energy devices for applications in IoT, wireless sensors, and other microelectronic systems due to their small footprints. In this work, the dimensional scaling of fully-integrated additively-fabricated MSCs is systematically investigated. The dimensions of the MSCs are scaled by varying the length and cross-section of their electrodes to study their scalability to the mm³ range, making them attractive for even chip-scale embedding. MSCs with the thickest electrodes demonstrate the highest values of capacitance and energy density, while MSCs with the thinnest electrodes show lower capacitance and energy densities, but deliver higher power densities. We observe that as expected, capacitance scales with dimensions. We observe excellent performance levels, including maximum areal capacitance of ~731.7 mF cm^{-2}, areal energy density of ~36.59 μW h cm^{-2}, areal power density of ~2669.8 mW cm^{-2}, and ~95% capacitance retention after 17 000 cycles. These MSCs also show maximum volumetric capacitance, volumetric energy density, and volumetric power density of 8.7 F cm^{-3}, 0.436 mW h cm^{-3}, and 31.78 W cm^{-3}, respectively. Overall, these are the highest values reported to date for such systems. These results are achieved by utilizing novel chemistries for the components of the MSCs and from tuning their geometry. The electrodes of the MSCs are formed from a nanocomposite of edge-oxidized graphite oxide (EOGO)/cerium oxide nanoparticles to benefit from both electrical double-layer capacitance (EDLC) and pseudocapacitance, the electrolyte is a UV-curable hydrogel based on (poly(ethylene glycol) diacrylate (PEGDA) + LiCl + lithium phenyl-2,4,6-trimethylbenzoylphosphinate (LAP) + water), and the current collector is a silver paste. These MSCs are fully packaged and sealed by 3D printing a package using polycaprolactone (PCL) and depositing a UV-curable resin-based encapsulant. Our findings demonstrate that such devices can be scaled to mm³ volumes while continuing to deliver excellent performance, making them attractive candidates for a range of embedded energy storage applications.

aLaboratory for Advanced Fabrication Technologies, Institute of Electrical and Microengineering, École Polytechnique Fédérale de Lausanne (EPFL), Neuchâtel 2002, Switzerland. E-mail: vivek.subramanian@epfl.ch

bDepartment of Electrical Engineering and Computer Sciences, University of California, Berkeley, CA, 94720-1770, USA

† Electronic supplementary information (ESI) available: Dimensional scaling details of the MSCs, thermogravimetric analysis (TGA) plots of electrode active material and the EOGO powder, TGA and Differential Scanning Calorimetry (DSC) curves of the silver paste used for 3D printing of the current collector, XRD PDF files of graphite and CeO_2 showing their corresponding characteristic peaks, XPS spectroscopy data of the electrode active material, nitrogen gas adsorption/desorption measurement of the electrode active material, the conductance as a function of heat treatment temperature for the silver current collector, the calculations for the electrochemical performance evaluations, the calculations of the kinetics of charge storage mechanisms, and the EIS measurments of the MSC (ID: L2) before and after 17 000 of charge/discharge cycles (Nyquist plots and the Randles equivalent circuit calculations) are listed in the ESI. See DOI: https://doi.org/10.1039/d3ta07159f

Introduction

Microsupercapacitors (MSCs) are small-scale (mm to cm-scale) energy storage devices that have attracted attention for use in numerous untethered microelectronic systems and are ultimately foreseen to replace/complement micro-batteries in such systems.[1,2,3,4,5] They have been used in versatile systems, such as soft robots,[6] wearable electronics,[7,8,9] and they possess potential applications for Internet of Things (IoT),[10] to name a few, acting as energy storage devices. Wide ranges of materials, such as carbonaceous materials,[11,12] metal oxides,[13,14] MXenes,[15,16] and conductive polymers[17,18] have been used in these systems as the electrode active materials with the aim to maximize the performance of these systems. Depending on the energy and power requirements of the specific microelectronic system, their energy storage/delivery systems should be custom designed.[19] This customization is particularly important as it determines the physical form factor as well as the electrical performance of the energy storage component.

This journal is © The Royal Society of Chemistry 2024

J. Mater. Chem. A, 2024, **12**, 10229–10241 | **10229**

The physical dimensions of energy storage devices plays a decisive role in determining their usability in different microelectronics applications.[20,21] Depending on needs of the target application, it is crucial to fabricate these energy storage systems with the appropriate footprint while fulfilling the requisite power and energy requirements. Given the interest in integration within microelectronic systems, there have been numerous reports on the fabrication of microsupercapacitors through rapid and flexible fabrication methods,[12,22,23,24,25] on the other hand, the realized devices have generally been larger than mandated by real application demands, and dimensional scaling studies on these systems have been very rare. There have been some dimensional scaling studies performed on microsupercapacitors, but these have been mostly focused on microsupercapacitors fabricated through conventional subtractive microfabrication techniques, and the electrodes used (carbon nanofibers,[26] graphene[27] and RuO_2 (ref. 28)) have not realized state of the art performance levels. While dimensional scaling studies have been performed on printed micro-batteries,[19,20,29] few such studies have been reported for printed microsupercapacitors, and the performance has been far below state of the art so far,[30] leaving performance wanting for real applications. To the best of our knowledge, no dimensional scaling study on hybrid microsupercapacitors, which deliver both electrical double-layer capacitive (EDLC) (i.e., usually stemming from carbonaceous materials) and pseudocapacitive charge storage mechanisms (i.e., stemming from conductive polymers, metal oxides, metal carbides, etc.) and, more specifically, which are fully additively fabricated, have been reported in the literature. Such hybrid systems represent the current state of the art in terms of microsupercapacitor performance,[31] and therefore, scaling studies are highly warranted.
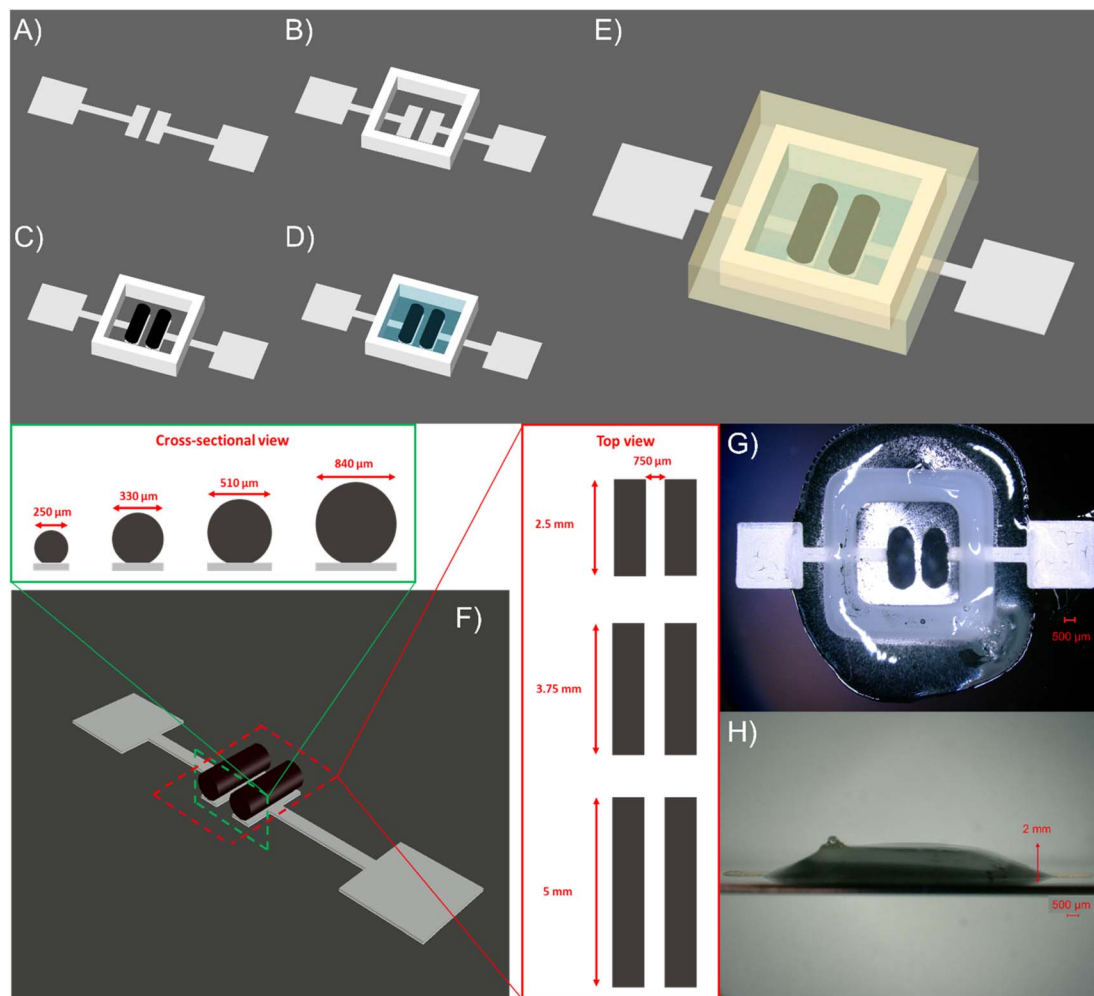
In this study, for the first time in the literature, we systematically study sub-mm^3 dimensional scaling of all-additively-fabricated ultra-small planar microsupercapacitors (MSCs), offering high energy and power density, by utilizing both EDLC and pseudocapacitive charge storage mechanisms. The study utilized 3D printed electrodes with control of both their length and cross-section; this is specifically important as fabricating microsupercapacitors with thick and porous electrodes is seen as a potential way to increase the energy density of these systems.[32] The MSCs show excellent performance—areal capacitance of ~731.7 mF cm^{-2}, maximum energy density of ~36.59 μW h cm^{-2}, and maximum power density of ~2669.8 mW cm^{-2}, and ~95% capacitance retention after 17 000 cycles, for an MSC possessing 3.75 mm-long electrodes printed with a nozzle of 840 μm diameter. We achieve these remarkable levels of performance through systematical dimensional scaling of the components of the MSCs by using novel chemistries for the components of the MSCs, which we have reported in our recent work.[31] Our electrode active material is a nanocomposite of edge-oxidized graphite oxide (EOGO)/cerium oxide nanoparticles (NPs) (~95 wt% EOGO–~5 wt% cerium oxide (ceria) NPs) which simultaneously benefits from both EDLC and pseudocapacitance. The electrode ink used for 3D printing only contained this nanocomposite dispersed in water without using any binders, organic additives, or rheology modifiers. We use a UV-curable hydrogel electrolyte based on (poly(ethylene glycol) diacrylate (PEGDA) + LiCl + lithium phenyl-2,4,6-trimethylbenzoylphosphinate (LAP) + water). The current collector is a silver paste. The dimensions of the MSCs are scaled by varying the length of the electrodes and the diameter of the nozzles with which the electrodes are 3D printed to vary their cross-sections. The MSCs are fully packaged and sealed by printing a package using poly caprolactone (PCL) and depositing a UV-curable resin-based encapsulant, respectively, to a maximum height of ~2 mm. We thus are able to study the dimensional scaling of a fully-integrated MSC delivering state of the art levels of performance down to the mm^3 scale.

Fabrication of microsupercapacitors and designing their dimensional scaling

We additively fabricated the planar MSCs via a combination of fused deposition modeling (FDM) and extrusion-based 3D printing following the procedures reported in our recent research article. Fig. 1 exhibits the printing procedure of the MSCs and the dimensional scaling methodology. We started with extrusion-based 3D printing of the current collectors using a silver paste (DELO-Dualbond IC343) on wet-oxidized silicon wafer (Fig. 1A). The current collector patterns resemble a parallel plate configuration such that two finger (i.e., plates) are located at known distance from each other (750 μm for all our MSCs). After printing, the current collectors were heat treated in air at 450 °C for 10 min. We optimized this heat treatment regime based on electrical resistivity measurements of the current collectors after heat treatments using a four-point probe setup (details of the electrical resistivity as a function of heat treatment temperatures and duration in ESI†). Next, we FDM printed the package walls around the fingers of the current collectors using polycaprolactone (PCL) (Fig. 1B). We then extrusion 3D printed the electrodes on the fingers of the heat treated current collectors without any following post treatments (Fig. 1C). Next, a UV-curable electrolyte based on (poly(ethylene glycol) diacrylate (PEGDA) + LiCl + lithium phenyl-2,4,6-trimethylbenzoylphosphinate (LAP) + water) was deposited in the interior space of the package walls to fully immerse the electrodes. This was followed by UV curing to form a hydrogel electrolyte and to consolidate the components (Fig. 1D). Finally, we deposited a UV-curable resin-based encapsulant (DELO Dualbond AD 761—a modified epoxy resin) on top of the UV cured electrolyte. This was also followed by a UV curing step to fully seal the MSCs (Fig. 1E). As shown in Fig. 1F, we designed the dimensional scaling study in such a way that the performance of the MSCs are evaluated as a function of change in the length of the electrodes and also the inner diameter of the nozzles with which the electrodes are 3D printed, which changes the electrode cross-section. The electrodes are 3D printed at three levels: 2.5 mm, 3.75 mm, and 5 mm. The inner diameters of the nozzles used to 3D print these electrodes are 250 μm, 330 μm, 510 μm, and 840 μm. Thus, the smallest active volume (including the electrodes and the inter-electrode gap) of the fabricated microsupercapacitors is under 1 mm^3. A more

10230 | J. Mater. Chem. A, 2024, 12, 10229–10241

This journal is © The Royal Society of Chemistry 2024

Fig. 1 The Schematics of the fabrication steps of the microsupercapacitors, (A) extrusion-based 3D printing the current collectors on a wet-oxidized silicon wafer using a silver paste and subsequently, heat treating the current collectors, (B) FDM printing of the package using PCL, (C) extrusion-based 3D printing of the electrodes on the current collectors (inside the package space), (D) deposition of UV-curable electrolytes inside the package to immerse the electrodes and subsequently, UV curing the electrolyte, (E) deposition of an encapsulant on top of the UV-cured electrolyte and subsequently UV curing it, (F) illustration of the design of dimensional scaling of the microsupercapacitors by changing the diameter of the nozzles used to 3D print the electrodes with different lengths, (G) a top view image of one of the fully 3D printed micro-supercapacitors (nozzle diameter of 840 μm and electrode length of 2.5 mm), and (H) a side view image the same fully 3D printed micro-supercapacitor as in (G) scale bars are 500 μm.

detailed description of the dimensional scaling of the MSCs is provided in Table S1 (ESI).†

Results and discussion

Chemistries of the components of the microsupercapacitors

As described in our previous work,[31] the electrode active material is a nanocomposite of edge-oxidized graphite oxide (EOGO)/cerium oxide (ceria) nanoparticles (NPs). We selected EOGO as it provides a combination of attractive properties—providing graphitic sheets with an almost intact sp^2 carbon basal plane resembling that of graphene in addition to proper dispersion in polar suspension media such as water due to the presence of oxygen containing functional groups at the edges of its planes.[33,34] We anchored ceria NPs, with sizes smaller than 5–10 nm, onto EOGO through an *in situ* synthesis procedure to

introduce the intrinsic electrochemical properties of these particles to the resultant nanocomposite. Ceria is one of the most abundant and least expensive rare-earth metal oxides, and it has shown promising redox reactivity as the active electrode material for supercapacitors.[35,36] We formulated the electrode inks using a nanocomposite of EOGO/ceria NPs (~95 wt% EOGO–~5 wt% ceria NPs) dispersed in water without using any organic additives, binders, or rheology modifiers. The novel chemistry of our electrode inks provides a hybrid system delivering both electrical double-layer capacitance (EDLC) (stemming mostly from EOGO sheets) and pseudocapacitance (originating mostly from ceria NPs). Fig. 2A shows the XRD patterns of the bare EOGO powder and the air-dried electrode ink. The concurrent presence of the sharp peak at ~26° and the wide and less intense peak at ~13° in the XRD pattern of the bare EOGO corresponds to its almost intact sp^2 graphitic basal

This journal is © The Royal Society of Chemistry 2024

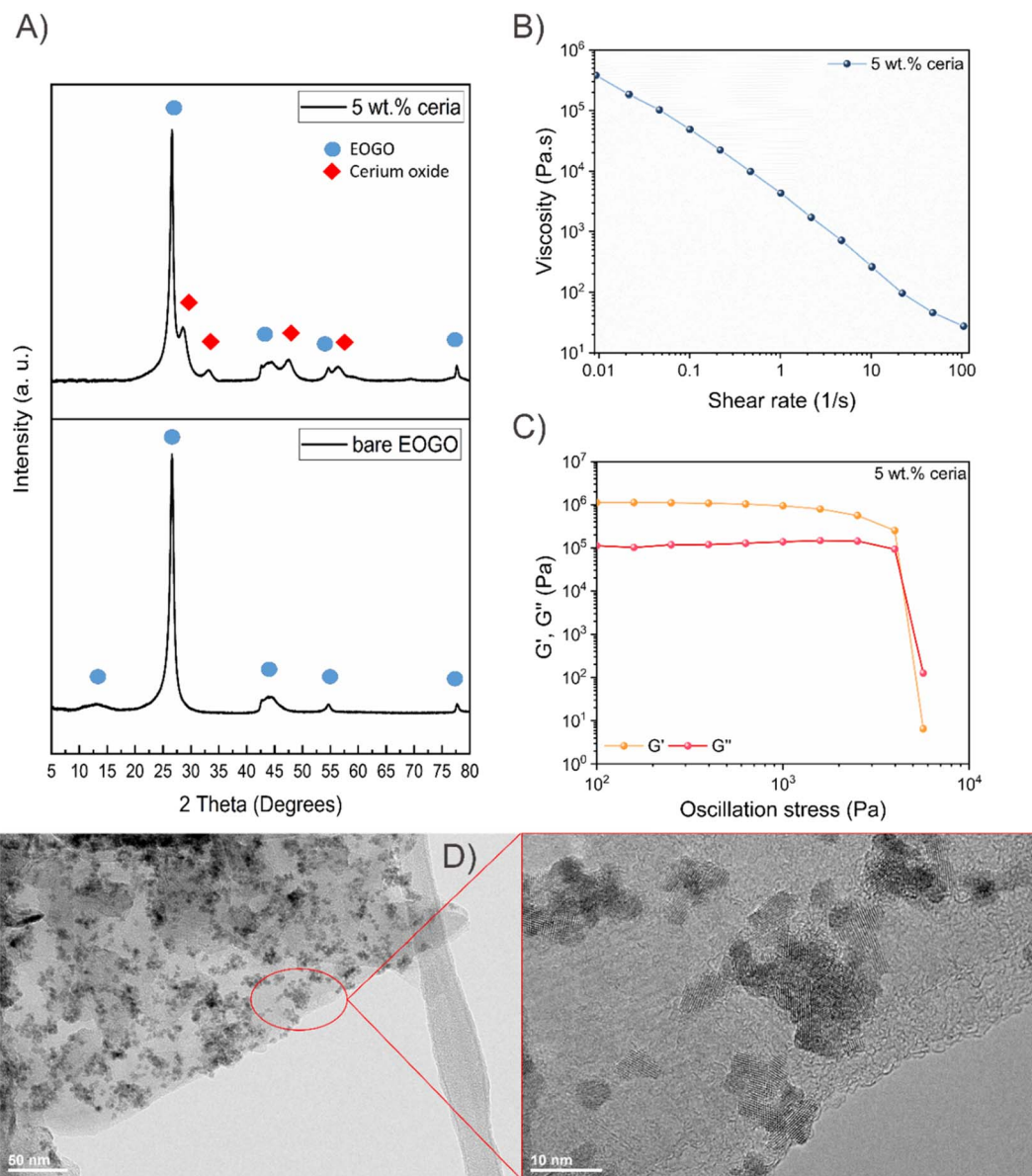*J. Mater. Chem. A*, 2024, **12**, 10229–10241 | **10231**

Fig. 2 (A) XRD characterization of the bare EOGO powder and the air-dried electrode ink comprising 5 wt% ceria nanoparticles, rheological characterizations of the aqueous electrodes ink (EOGO/ceria nanocomposite—5 wt% ceria nanoparticles) (B) viscosity as a function of shear rate, (C) oscillation measurement demonstrating the storage modulus (G′) and the loss modulus (G″) of the same ink as a function of oscillation stress, and (D) TEM images of the air-dried electrodes, the same used for XRD characterization as shown in (A).

plane and the presence of oxygen-containing functional groups on its edges.[33] The XRD pattern of the air-dried electrode ink shows the formation of CeO_2 crystalline phase.[37,38]

We also investigated the rheological characterizations of the aqueous electrode ink as shown in Fig. 2B and C. The aqueous electrode ink demonstrated a shear-thinning behavior—decrease in its viscosity as a function of increase in shear rate (Fig. 2B), and a viscoelastic behavior with a more dominant G′ (storage modulus, *i.e.*, elastic behavior) values than G″ (loss modulus, *i.e.*, viscous behavior) before their intersection point (known as the flow point) (Fig. 2C), which are all indicators of the suitability of the ink for extrusion-based 3D printing.[39] Changing the shear rate from 0.01 Pa s to 100 Pa s, the viscosity

of the ink significantly dropped (by almost four orders of magnitude). The oscillation rheometry showed that the G′ of the electrode ink in the linear viscoelastic region is almost one order of magnitude larger than its G″. We also investigated the morphological details of the EOGO/ceria NPs nanocomposite using TEM imaging as shown in Fig. 2D. Crystalline ceria NPs with sizes of less than 5–10 nm are anchored onto the EOGO sheets and they quite uniformly distributed on the surface of the EOGO sheets. The electrode active material (*i.e.*, EOGO (∼95 wt%)/cerium oxide NPs (∼5 wt%)) showed a specific surface area of ∼284 m^2 g^{-1} (N_2 adsorption/desorption plot in ESI†).

10232 | *J. Mater. Chem. A*, 2024, **12**, 10229–10241

This journal is © The Royal Society of Chemistry 2024

We formulated a UV-curable hydrogel electrolyte based on (poly(ethylene glycol) diacrylate (PEGDA) + LiCl + lithium phenyl-2,4,6-trimethylbenzoylphosphinate (LAP) + water). LiCl has been widely employed in electrolytes of printed micro-supercapacitors.[40,41,42,43] PEGDA[44,45,46] and LAP (a water-soluble photo-initiator)[47,48,49] have been commonly utilized in 3D printing of hydrogels. By combining these, the resultant electrolyte showed a gel structure after UV curing, providing suitable mechanical stability in the MSCs eliminating the need for a separator between the electrodes.[50] The chemical composition and processing condition for the electrolyte was set to a total LiCl concentration of (1.6 M), while the concentration of the PEGDA was set to 0.08 g ml^{-1} and the concentration of LAP was 0.16 wt% (by weight of PEGDA) that was cured for 20 seconds by a 365 nm UV lamp (these concentrations are calculated based on a 25 ml total volume of the electrolyte).

For FDM printing the package walls, we used poly-caprolactone (PCL). PCL is a biocompatible polymer with a low melting temperature and a hydrophobic nature.[51] The main reason for printing the package walls is that it acts as a container for the electrolyte before it is UV-cured.

We encapsulated the MSCs in order to enhance their stability to ensure that the electrolyte is not evaporated over time. We used a modified epoxy-based resin, which is UV-curable. The encapsulant was UV cured using a 405 nm UV lamp for 60 seconds.

Performance evaluation of the microsupercapacitors

We systematically investigated the electrochemical performance of the microsupercapacitors as a function of their dimensions (*i.e.*, length of the electrodes, and the diameter of the nozzle with which they are printed). In order to investigate how changing the dimensions influences the charge–discharge behavior of the MSCs, we performed galvanostatic charge–discharge (GCD) measurements on MSCs with varying dimensions. As shown in Fig. 3A–D, by a simultaneous increase of the length of the electrodes, and the nozzle size used for printing the electrodes, the duration of full cycle of charge–discharge was increased. For example, a full charge–discharge cycle at a current of 50 μA took ∼175 s for an MSC printed 250 μm nozzle and electrode length of 5 mm, while for the MSC comprising a 5 mm long electrode printed with a 840 μm nozzle,
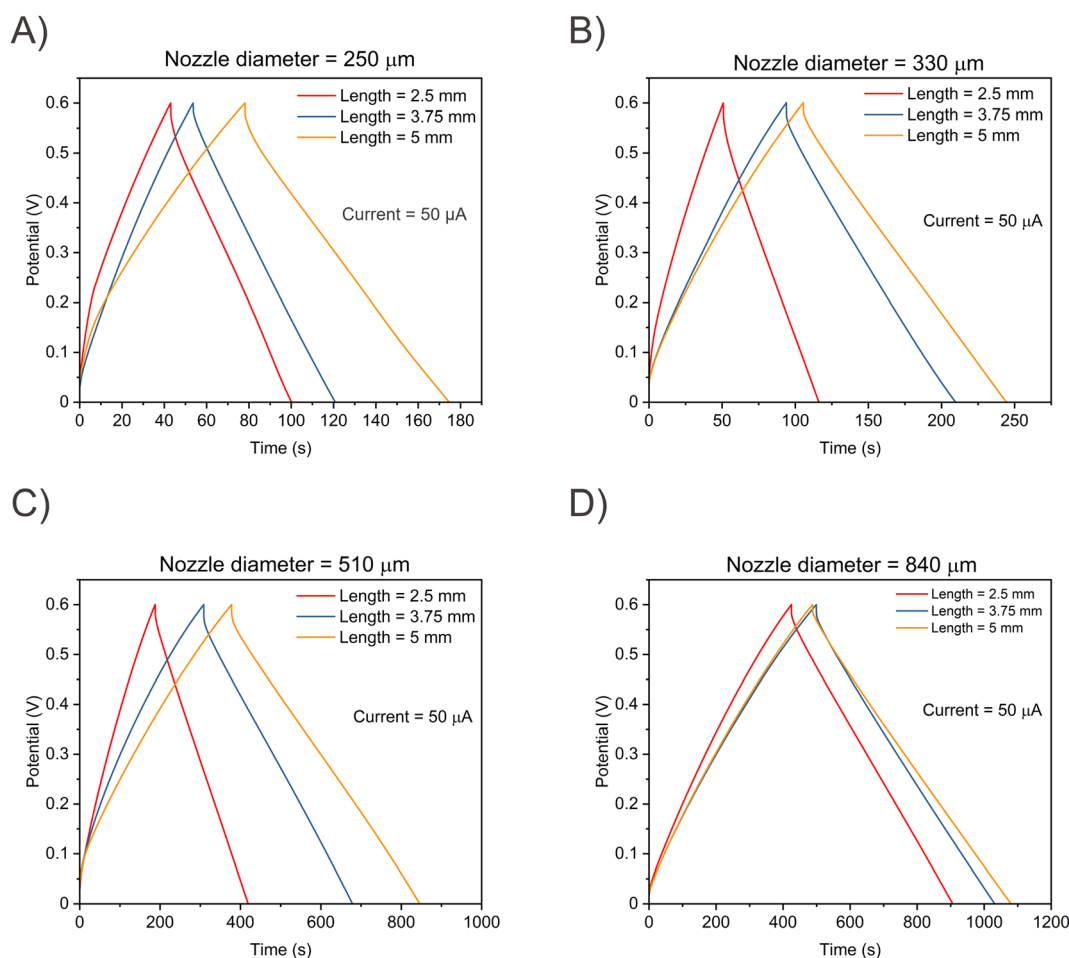

Fig. 3 Galvanostatic charge−discharge diagrams of the additively fabricated MSCs as a function of electrode length and the nozzle diameter with which the electrodes are printed, (A) nozzle diameter: 250 μm, (B) nozzle diameter: 330 μm, (C) nozzle diameter: 510 μm, (D) nozzle diameter: 840 μm.

This journal is © The Royal Society of Chemistry 2024

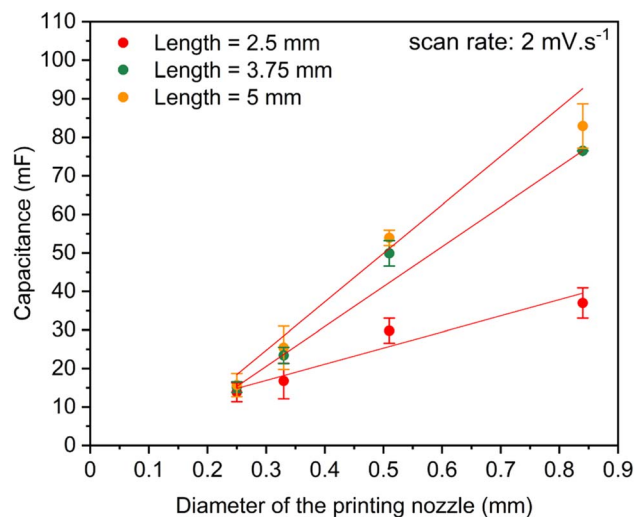*J. Mater. Chem. A*, 2024, **12**, 10229–10241 | **10233**

Fig. 4 Capacitance (non-normalized per area or volume) of all the MSCs as a function of their electrode length and the diameter of the nozzle used for printing them.

a full cycle takes ~1140 s. These results demonstrate that, as expected, longer electrodes printed with larger nozzle diameters realize higher capacitance levels due to their larger active volumes and larger overall surface area of the active materials available in these electrodes.

We further investigated the electrochemical properties of the MSCs by cyclic voltammetry (CV). As shown in Fig. 4, capacitance of the MSCs scales with the length of the electrodes and the diameters of the nozzle with which they are printed. At each nozzle diameter level, increase in the length of the electrode resulted in an increase in the capacitance of the MSCs, as expected by pure dimensional scaling laws. This is due to the greater increase in the active surface area when electrodes become thicker and longer. This observation is in agreement with the results from GCD measurements discussed earlier.

We used electrochemical impedance spectroscopy (EIS) measurements to calculate the equivalent series resistance (ESR) of the MSCs (examples of EIS plots of the MSCs are shown in ESI†). Fig. 5A illustrates the ESR of the MSCs as a function of the length of the electrodes and the printing nozzle diameter used for them. ESR, also known as the internal resistance, is an indication of the total resistance of the system—defined as the sum of the bulk electrolyte resistance, the resistance of the electrode, and the contact resistance between the electrode and the current collector.[52] It is one of the important performance metrics of MSCs since it correlates to how much internal energy loss a system has. We observed that at each nozzle diameter, increasing the length decreased the ESR of the MSCs, which is expected, since this effectively realizes a capacitor with a larger "plate". We also observed that electrodes printed with larger nozzle diameters showed smaller ESR values. Again, this is expected, since increasing the length and the thickness of the electrodes increases the available surface. Hence, lower values

of ESR are obtained for longer and thicker electrodes. All the ESR values obtained for the MSCs are less than ~90 Ω.

We further studied the dependence of the kinetics of charge storage of the MSCs on their dimensions. As shown in Fig. 5B, we compared the charge storage kinetics of the MSCs with 3.75 mm long electrodes printed with the smallest (i.e., 250 μm) and largest (i.e., 840 μm) nozzles (the details of the calculations in ESI†). The inks that are extrusion 3D printed experience substantial shear stresses at the wall of the printing nozzles and these shear stresses are increased by decreasing the nozzle dimeter.[53] Therefore, the shear stress at the wall of the nozzle of 250 μm diameter was the highest, and in case of printing the electrodes with the printing nozzle of diameter 840 μm, the shear stress at the wall of the nozzle was the lowest. It has been shown that the shear stress at the wall of the printing nozzle causes the graphitic sheets to align along the printing direction.[54,55] Thus, due to higher shear stresses at the walls of the nozzles with smaller diameters, the graphitic sheets align more strongly along the printing direction resulting in lower surface roughness/porosity at the outmost surface of the printed electrodes.[56] For the same reason, lower shear stresses are experienced by the graphitic sheets during printing with larger nozzles, hence, these printed electrodes could possess higher surface roughness/porosity at their outmost surface as the graphitic sheets experience less alignment. The kinetic study of the charge storage also demonstrates the increase in the diffusion-controlled charge storage (i.e., slow kinetic charge storage mechanism) in thicker electrodes possibly due to more available diffusion pathways, which might be due to higher surface roughness/porosity at the outmost surface of these electrodes. This observation further emphasizes that even with the same chemistry of electrodes, the printing conditions (such as nozzle diameter) can significantly affect the charging kinetics of the resultant 3D printed MSCs.

Fig. 5C exhibits the cyclic life of the MSC comprising 3.75 mm long electrodes printed with the 840 μm nozzle achieved by GCD measurements. A remarkable cyclic life—94.98% capacitance retention after 17 000 cycles at a current of 600 μA was realized. Each cycle took almost 50 seconds and in total the cyclic life test was going nonstop for ~230 hours. Fig. 5D shows the GCD diagrams of the 1st and the 17000th cycles and shown that there is not a significant change in the shape of the diagrams. The increase in the capacitance after ~13 000 cycles of charge/charge at this current (600 μA) may be attributed to surface activation of the electrode coupled with the diffusion of ionic species of the electrolyte in the pores of the electrode materials[57] and/or to introduction of new surfaces by (partial) exfoliation of graphitic sheets as a result of shrinkage/expansion of the electrode materials through the charge/discharge process.[58]

We continued with performing CV and GCD measurements at different scan rates and currents, respectively, on the MSCs possessing 3.75 mm long electrodes printed with 250 μm and 840 μm nozzles (Fig. 6A–D). As shown in Fig. 6A and B, the CV curves were collected at scan rates ranging from 2 mV cm^{-2} to 250 mV cm^{-2}. Unlike the MSC printed with the 840 μm nozzle,

10234 | J. Mater. Chem. A, 2024, 12, 10229–10241

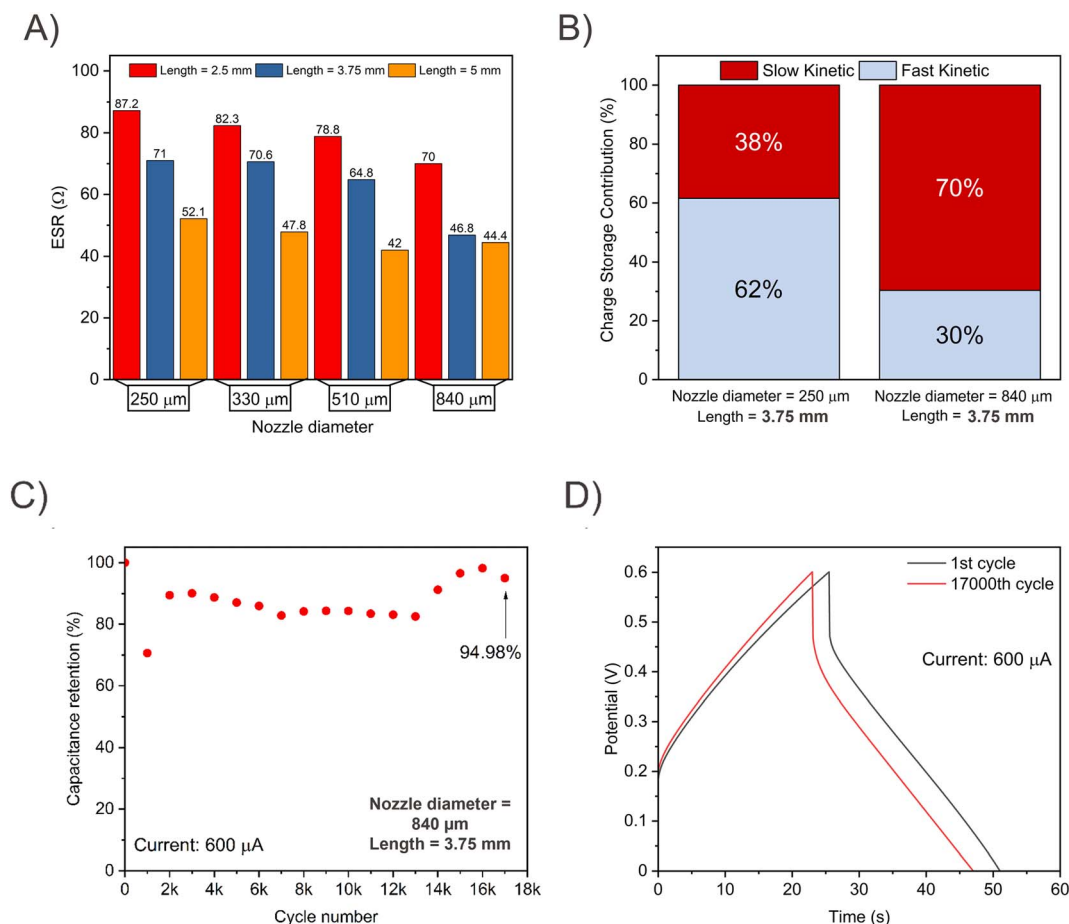This journal is © The Royal Society of Chemistry 2024

Fig. 5 (A) the ESR values of the MSCs, (B) kinetic study of charge storage of two of the fabricated MSCs with 3.75 mm long electrodes printed with the smallest (*i.e.*, 250 μm) and the largest (*i.e.*, 840 μm) nozzles, (C) cyclic life of the MSC possessing 3.75 mm long electrodes printed with a 840 μm nozzle, and (D) GCD plots of the same MSC showing the 1st and the 17000th charge/discharge cycles.

the MSC printed with the 250 μm nozzle showed a better scan rate ability—the CV curves continued to get larger by increasing the scan rate. It can be inferred from this result that the MSC printed with the 250 μm nozzle could facilitate faster charge storage. This observation is also in agreement with the results of the kinetic study of charge storage where the MSC printed with the larger nozzle diameters showed more pronounced slow kinetic charge storage. We note that the CV and GCD curves show strong EDLC-like behavior, which is expected, since the ceria loading is only 5% and the observation of redox characteristics in the hybrid electrodes is therefore not dominant. Similar behavior has been observed in other similar systems.[36,38,59]

Fig. 6C and D exhibit GCD curves at different currents ranging from 50 μA to 500 μA. For both MSCs, by increasing the current, the duration of the full charge–discharge cycle was decreased. The GCD curves of the MSC printed with the 840 μm nozzle show longer durations at each given current. In agreement with the CV curves, this observation is also an indication that the capacitance values of the MSC printed with the 840 μm nozzle is larger than those of the MSC printed with the 250 μm nozzle. The areal and volumetric capacitance of these MSCs,

which were calculated by using their CV curves, are depicted in Fig. 6E and F. While the areal and volumetric capacitances (scan rates of 2 mV s^{-1} to 250 mV s^{-1}) of the MSC printed with the 840 μm nozzle ranged between 731.7–25.7 mF cm^{-2}, and 8.7–0.31 F cm^{-3}, respectively, the MSC printed with the 250 μm nozzle showed areal and volumetric capacitances of 194.68–40.94 mF cm^{-2}, and 7.79–1.64 F cm^{-3}, respectively.

We next compared the energy density and power density values of these MSCs with some of examples of printed MSCs from the literature as shown by the Ragone plot in Fig. 7. We used CV curves at different scan rates to calculate these performance metrics (details of calculations in ESI†). These examples include MSCs with electrodes of graphene-vanadium quantum dots/reduced graphene oxide (G–VNQDs/rGO),[42] Ag-polypyrrole,[60] MXene,[61,62] and graphene oxide/Ag NPs/CNT/MoS$_2$.[63] Our MSCs with electrodes of 3.75 mm of length which were printed with an 840 μm nozzle (MSC ID: L2) or a 250 μm nozzle (MSC ID: XS2) (more details on the MSCs IDs in ESI†) both showed a combination of high energy and power densities. The MSC printed with an 840 μm nozzle generally showed higher energy density values with a maximum energy density of 36.59 μW h cm^{-2}, however, it showed a sharp decrease in its
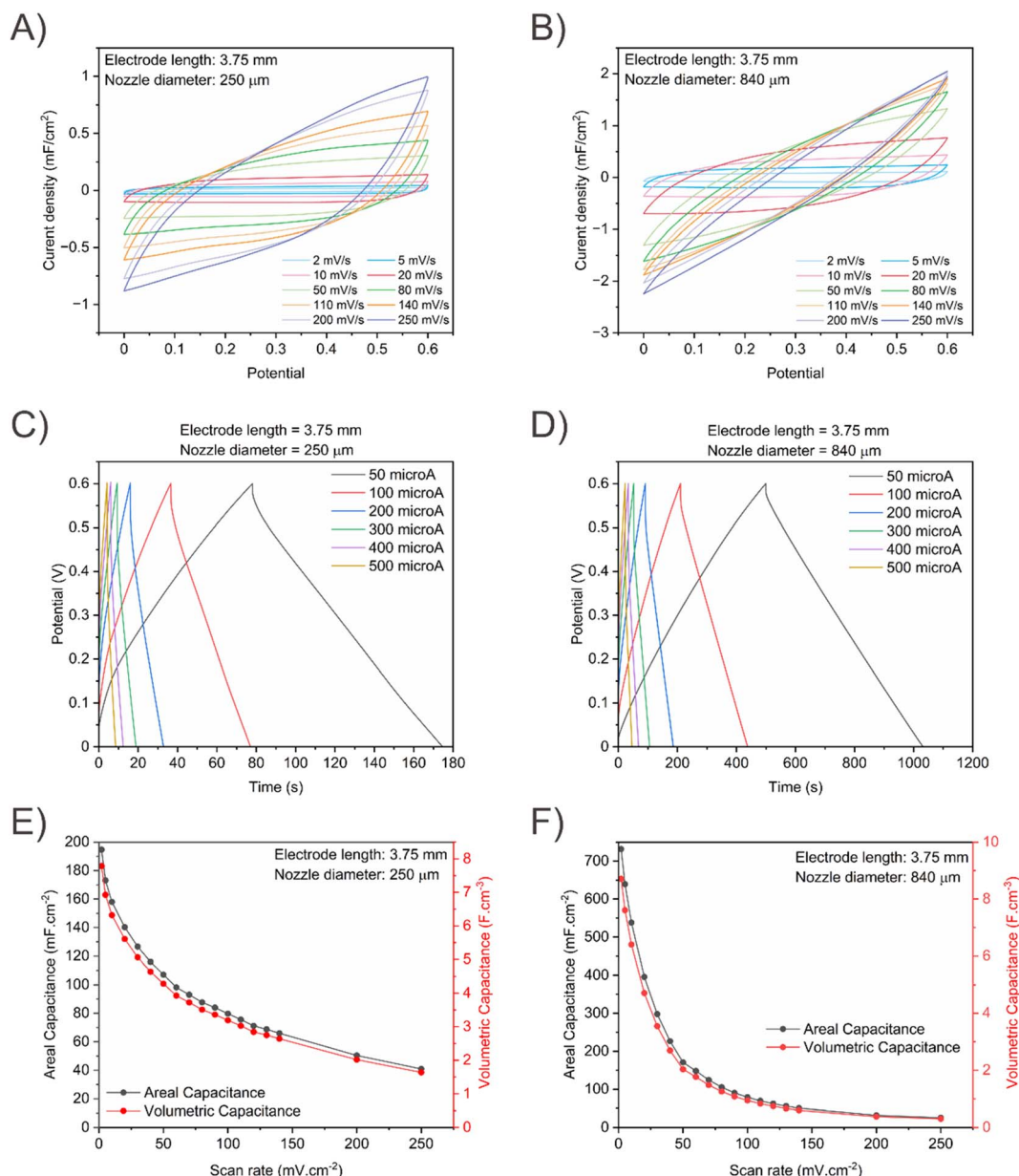
Fig. 6 CV curves of the MSCs with an electrode length of 3.75 mm and printed with a nozzle diameter of (A) 250 μm, and (B) 840 μm, and GCD curves with an electrode length of 3.75 mm and printed with a nozzle diameter of (C) 250 μm, and (D) 840 μm, and areal and volumetric capacitance values of the MSCS (as a function of scan rates used in CV measurements) with an electrode length of 3.75 mm and printed with a nozzle diameter of (E) 250 μm, and (F) 840 μm.

energy density at higher scan rates (points that are more on the right side of the plot for each reference correspond to higher scan rates). On the other hand, the MSC printed with the 250 μm nozzle showed higher power density values at higher scan rates, with a maximum value of 3070.77 mW cm^{-2}. Maximum volumetric energy and power densities of the MSC printed with the 250 μm nozzle are 0.389 mW h cm^{-3}, 122.8 W cm^{-3}, and for the MSC printed with the 840 μm nozzle are 0.436 mW h cm^{-3}, and 31.78 W cm^{-3}, respectively.

Such high levels of energy and power densities attest to the remarkable combination of performance of our MSCs compared to examples of MSCs from the literature.

We also compared the areal energy and power densities of our microsupercapacitors with results from the literature. The set of comparison encompasses microsupercapacitors with electrode thicknesses ranging from nm-scale up to μm-scale. It should be noted that when a comparison of the performance of microsupercapacitors are made, their geometrical features (e.g., electrode thickness) should be mentioned. While the thickness of the electrodes in our microsupercapacitors range between 250 μm and 840 μm, the thickness of the electrodes in the selected examples form the literature are as follows: 412 μm,[42] 3.97 μm,[60] 1.4–18 μm,[61] 530 ± 120 nm,[62] and 500–2000 μm.[63]

10236 | J. Mater. Chem. A, 2024, **12**, 10229–10241

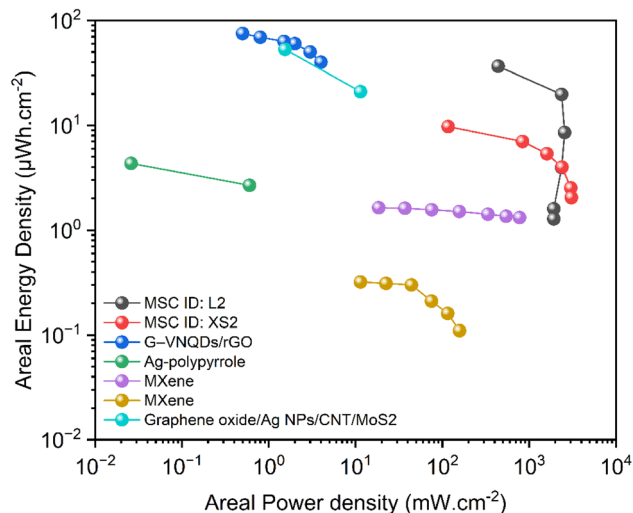This journal is © The Royal Society of Chemistry 2024

Fig. 7 Ragone plot exhibiting areal energy and power densities of our MSCs possessing an electrode length of 3.75 and printed with nozzle diameters of 250 μm and 840 μm in comparison with some of the selected examples of printed MSCs from literature.

Conclusions

In summary, we systematically studied the effects of dimensional scaling on the performance of all-additively fabricated encapsulated hybrid MSCs. We observed that capacitance scales with dimensions, as expected. Moreover, we achieved a remarkable combination of performance levels included a realized areal capacitance of ~731.7 mF cm^{-2}, energy density of ~36.59 μW h cm^{-2}, power density of ~2669.8 mW cm^{-2}, ~95% capacitance retention after 17 000 cycles, and maximum volumetric capacitance, volumetric energy density, and volumetric power density of 8.7 F cm^{-3}, 0.436 mW h cm^{-3}, and 31.78 W cm^{-3}, respectively. Our results show that appropriately designed microsupercapacitors can deliver high performance even when scaled to mm^3 volumes, and emphasize the importance of dimensional scaling of printed MSCs in addition to the selection and optimization of components' chemistries to tune their capacitive performance.

Experimental section

Chemicals

Edge-oxidized graphite oxide (EOGO) was purchased from Garmor Inc. and cerium nitrate hexahydrate (99% trace metals basis), sodium hydroxide (anhydrous, reagent grade, ≥98%), lithium chloride (ACS reagent, ≥99%), poly(ethylene glycol) diacrylate (average M_n 700) were purchased from Sigma-Aldrich. Lithium phenyl-2,4,6-trimethylbenzoylphosphinate (LAP) (99%) was purchased from Apollo scientific. All chemicals were used as received without further modifications. We purchased a commercial silver paste (DELO-DUALBOND IC343) from DELO and used it for the fabrication of the current collectors. We used a commercial UV-curable encapsulant (DELO Dualbond AD 761) for encapsulation of the MSCs.

Synthesis of edge-oxidized graphite oxide (EOGO)/ceria nanocomposite and electrode ink preparation

We synthesized the edge-oxidized graphite oxide (EOGO)/ceria nanocomposites by a facile sonochemical method described in our previous work.[31] For the synthesis of the EOGO/ceria nanocomposite (~5 wt% ceria–95 wt% EOGO, determined by TGA measurements), we dispersed EOGO (2.5 g) in deionized water (50 ml). We sonicated this suspension in a sonication bath for 15 min (mixture I). After this step and while sonication was continued, an aqueous solution of cerium nitrate hexahydrate (25 ml of 0.0625 M) was added (in increments of 500 μl) to the EOGO suspension within 15 min (to make mixture II). Then, we continued the sonication for another 15 min while adding an aqueous solution of sodium hydroxide (25 ml of 0.0625 M) to this mixture (increments of 250 μl) (to make mixture III). Afterwards, we continued the sonication of the mixture III for 2 hours (to make mixture IV). At the end of the sonication procedure, the mixture IV was poured into 50 ml centrifuge tubes for centrifugation at 10 000 rpm for 15 minutes at 4 °C. The centrifugation of the mixture IV was repeated three more times under the same conditions, with intermediate disposal of the supernatant and redispersion of the solid between centrifugation steps, until the pH of the supernatant went above ~6. At the end of the last centrifugation step, we collected the pastes at the bottom of the centrifuge tubes and transferred them to 3 ml barrels without further modifications for 3D printing the electrodes.

Preparation of the UV-curable electrolytes

10 ml solutions of poly(ethylene glycol) diacrylate (PEGDA) with a concentration of 0.2 g ml^{-1} were prepared. Then, 10 ml solutions of LiCl at concentration of (4 M) was prepared. The LiCl solution was added at once to the PEGDA solution and stirring was continued for 30 min at 50 °C (mixture I). Then, 5 ml solutions of lithium phenyl-2,4,6-trimethylbenzoylphosphinate (LAP) (0.8 wt% by weight of PEGDA) was prepared and this solution was added to mixture I to make the UV-curable electrolyte to a total volume of 25 ml.

3D printing of the MSCs

We printed the MSCs by a combination of extrusion-based 3D printing and fused deposition modeling (FDM) printing on a multi-head 3D printer (BioX6-Cellink) equipped with six different heads as described in our previous work.[31] We started 3D printing of the MSCs first by printing the current collectors on a wet-oxidized silicon wafer using one of the pneumatically pressurized heads on the 3D printer. We used a commercial silver paste (DELO-DUALBOND IC343) for printing the current collectors. The current collectors were printed at room temperature using a nozzle with an inner diameter of 100 μm (6.35 mm nozzle length). The printing pressure and printing speed were 5.4 bar and 2 mm s^{-1}, respectively. After the printing of the current collectors, the printed patterns were heat treated at 450 °C for 10 in air in a muffle furnace (Thermo SCIENTIFIC F6020C-33-80) (this heat treatment temperature and duration was selected as it resulted in the lowest sheet resistance of the

This journal is © The Royal Society of Chemistry 2024

J. Mater. Chem. A, 2024, **12**, 10229–10241 | **10237**

printed current collectors – see Fig. S17 in the ESI†). Next, we FDM printed the package walls using polycaprolactone (PCL) surrounding the fingers of the current collectors. The nozzle inner diameter, nozzle temperature, printing pressure and printing speed were set to 410 μm, 140 °C, 5.7 bar, and 1 mm s^{-1}, respectively. Next, we deposited the electrode aqueous ink (edge-oxidized graphite oxide (EOGO)/ceria NPs nanocomposites (∼95 wt%–∼5 wt%) + water) on the fingers of the current collectors through extrusion-based 3D printing at room temperature. We used nozzles with an inner diameters of 250 μm, 330 μm, 510 μm, 840 μm (all with a 6.35 mm nozzle length), and we set the printing pressure and speed to 1.5–3 bar, and 3 mm s^{-1}, respectively. Then, we deposited a UV-curable electrolyte (poly(ethylene glycol) diacrylate (PEGDA) + LiCl + lithium phenyl-2,4,6-trimethylbenzoylphosphinate (LAP) + water) through a nozzle with inner diameter of 1 mm in the interior space inside the package walls to immerse the electrodes. Subsequently, we UV cured the electrolyte for 20 s using a UV curing head on the 3D printer (UV wavelength of 365 nm) from a 1.5 cm distance to cross-link and mechanically stabilize the structure. Afterwards, we deposited a UV-curable encapsulant (DELO Dualbond AD 761-a modified epoxy resin) on top of the cured electrolyte and around the exteriors of the package walls using a nozzle with an inner diameter of 1 mm. We then UV cured the encapsulant for 60 s using another UV curing head on the 3D printer (UV wavelength of 405 nm) from a 3 cm distance to fabricate the fully integrated MSCs.

Characterization

Thermogravimetric analysis (TGA) and dynamic scanning calorimetry (DSC) measurements were performed using a LINSEIS STA 1600 in air with a heating rate of 10 °C min^{-1} from room temperature up to 750 °C. As the EOGO electrode without ceria showed a residue of around 4 wt% at the end of the TGA measurement, we assumed this amount of EOGO to be present in the ceria-containing electrode material (we estimated the loading of the ceria NPs in the electrode by subtracting this residual weight (∼4 wt%) from the total residue of the ceria containing electrode). Electrical resistivity of the silver current collector material (i.e., silver paste) was measured using a four-point probe (LUCAS LABS 302) with a KEITHLEY 2601 SYSTEM Source Meter on squares patterns of 8 mm × 8 mm that were extrusion 3D printed on the wet-oxidized silicon wafer substrates and were heat treated at different temperatures and for different durations. We performed TEM imaging and energy dispersive X-ray spectroscopy (EDX) using an analytical TEM instrument (FEI Tecnai Osiris). We used Lacey/Carbon TEM grids (200 Mesh, Cu, LC200-Cu-25-Electron Microscopy Sciences) as the substrates for the observations. The acceleration voltage was set to 200 kV and the vacuum level in the column was 8.8e-008 Torr (1.18e-005 Pascal). We performed the rheological measurements on a rotational rheometer (DHR2-TA Instruments) using aluminum disposable parallel plates of diameter of 25 mm at a gap size of 1000 μm. For the oscillation measurements, we set the frequency to 10 rad s^{-1}, and we altered the oscillation stress from 0.01 to 6000 Pa. Moreover, for the viscosity measurements, the shear rate ranged

from 0.01 s^{-1} to 100 s^{-1}. For XRD measurements, the electrode sample (dried powder) and EOGO powder were deposited and spread over a single crystalline silicon substrate. The diffraction patterns were collected within a 2θ range of 5° to 80° at a scanning step size of 0.1° s^{-1}. XPS measurements were performed on the dried electrode ink on an Axis Supra (Kratos Analytical) machine using the monochromated Kα X-ray line of an aluminium anode. We set the pass energy of the XPS measurements to 40 eV with a step size of 0.15 eV. The samples were insulated from the sample holder and an electron flood gun was used to limit charging effects. Cerium peaks were fitted using CasaXPS according to E. Paparazzo.[64] We also performed nitrogen gas adsorption/desorption measurement on the electrode active material using a surface area analyzer (Anton-paar, autosorb iQ-adsorption analyzer) applying the Brunauer–Emmett–Teller (BET) method. The sample was first degassed under vacuum for 4 hours at a temperature of 200 °C. Then, nitrogen gas adsorption/desorption measurements were performed to find the values of specific surface area of the electrode materials using the BET method. It is worth mentioning that prior to running TGA, XRD, XPS, and nitrogen gas adsorption/desorption measurements, we dried the electrode ink and EOGO powder at room temperature under ambient conditions for 2 days and then obtained these samples in powder form to use them for the measurements.

We performed the electrochemical performance of the fully 3D printed MSCs (Cyclic Voltammetry (CV), Galavanostatic Charge/Discharge (GCD), and Electrochemical Impedance Spectroscopy (EIS) measurements) in a two-electrode setup using an electrochemical working station (Autolab PGSTAT 302, Metrohm) equipped with an impedance module (FRA32M) at room temperature. The CV measurements were performed at varying scan rates (2 to 250 mV s^{-1}) in the (0 V to +0.6 V) potential window. We collected the GCD curves were collected at different currents ranging from (50 μA to 500 μA). The EIS measurements were carried out at a frequency range from 100 mHz to 100 kHz at an amplitude of 0.01 V. We used the software Nova 2.1 (Metrohm) to fit the EIS data and extract the Randles equivalent circuit values.

Data availability

The data that support the findings of this study are available from the authors upon reasonable request.

Author contributions

Amin Hodaei: conceptualization, investigation, methodology, data curation, writing – original draft, writing – review & editing, visualization. Vivek Subramanian: conceptualization, resources, data curation, writing – review & editing, supervision.

Conflicts of interest

The authors declare that they have no known competing financial interests or personal relationships that could have appeared to influence the work reported in this paper.

10238 | J. Mater. Chem. A, 2024, 12, 10229–10241

This journal is © The Royal Society of Chemistry 2024

Acknowledgements

References

1 P. Simon and Y. Gogotsi, Materials for electrochemical capacitors, *Nat. Mater.*, 2008, **7**, 845–854, DOI: **10.1038/nmat2297**.

2 R. Kötz and M. Carlen, Principles and applications of electrochemical capacitors, *Electrochim. Acta*, 2000, **45**(15–16), 2483–2498, DOI: **10.1016/S0013-4686(00)00354-6**.

3 Y. Shao, *et al.*, Design and Mechanisms of Asymmetric Supercapacitors, *Chem. Rev.*, 2018, **118**(18), 9233–9280, DOI: **10.1021/acs.chemrev.8b00252**.

4 *Flexible Supercapacitor Nanoarchitectonics*, ed. I. namuddin, M. I. Ahamed, R. Boddula and T. Altalhi, Wiley-Scrivener, Hoboken, NJ, p. 2021.

5 P. Chang, H. Mei, S. Zhou, K. G. Dassios and L. Cheng, 3D printed electrochemical energy storage devices, *J. Mater. Chem. A*, 2019, **7**(9), 4230–4258, DOI: **10.1039/C8TA11860D**.

6 S. S. Nardekar and S. Kim, Untethered Magnetic Soft Robot with Ultra-Flexible Wirelessly Rechargeable Micro-Supercapacitor as an Onboard Power Source, *Adv. Sci.*, 2023, **10**(28), 2303918, DOI: **10.1002/advs.202303918**.

7 Y. Lu, K. Jiang, D. Chen and G. Shen, Wearable sweat monitoring system with integrated micro-supercapacitors, *Nano Energy*, 2019, **58**, 624–632, DOI: **10.1016/j.nanoen.2019.01.084**.

8 C. Zhang, *et al.*, High-energy all-in-one stretchable micro-supercapacitor arrays based on 3D laser-induced graphene foams decorated with mesoporous ZnP nanosheets for self-powered stretchable systems, *Nano Energy*, 2021, **81**, 105609, DOI: **10.1016/j.nanoen.2020.105609**.

9 S. Park, H. Lee, Y.-J. Kim and P. S. Lee, Fully laser-patterned stretchable microsupercapacitors integrated with soft electronic circuit components, *NPG Asia Mater.*, 2018, **10**(10), 959–969, DOI: **10.1038/s41427-018-0080-z**.

10 A. H. Mohd Aman, N. Shaari and R. Ibrahim, Internet of things energy system: Smart applications, technology advancement, and open issues, *Int. J. Energy Res.*, 2021, **45**(6), 8389–8419, DOI: **10.1002/er.6451**.

11 K.-H. Lee, S.-S. Lee, D. B. Ahn, J. Lee, D. Byun and S.-Y. Lee, Ultrahigh areal number density solid-state on-chip microsupercapacitors via electrohydrodynamic jet printing, *Sci. Adv.*, 2020, **6**(10), eaaz1692, DOI: **10.1126/sciadv.aaz1692**.

12 W. Zhang, *et al.*, From cotton to functional flexible transparent film for printable and flexible microsupercapacitor with strong bonding interface, *J. Mater. Chem. A*, 2023, **11**(17), 9504–9511, DOI: **10.1039/D3TA00623A**.

13 B. Bounor, B. Asbani, C. Douard, F. Favier, T. Brousse and C. Lethien, On chip MnO2-based 3D micro-supercapacitors with ultra-high areal energy density, *Energy Storage Mater.*, 2021, **38**, 520–527, DOI: **10.1016/j.ensm.2021.03.034**.

14 J. Lee, J. Y. Seok, S. Son, M. Yang and B. Kang, High-energy, flexible micro-supercapacitors by one-step laser fabrication of a self-generated nanoporous metal/oxide electrode, *J. Mater. Chem. A*, 2017, **5**(47), 24585–24593, DOI: **10.1039/C7TA07960E**.

15 M. Wang, *et al.*, Ultrastretchable MXene Microsupercapacitors, *Small*, 2023, **19**(21), 2300386, DOI: **10.1002/smll.202300386**.

16 S. Li, T.-H. Chang, Y. Li, M. Ding, J. Yang and P.-Y. Chen, Stretchable Ti $_3$ C $_2$ T $_x$ MXene microsupercapacitors with high areal capacitance and quasi-solid-state multivalent neutral electrolyte, *J. Mater. Chem. A*, 2021, **9**(8), 4664–4672, DOI: **10.1039/D0TA10560K**.

17 N. Kurra, M. K. Hota and H. N. Alshareef, Conducting polymer micro-supercapacitors for flexible energy storage and Ac line-filtering, *Nano Energy*, 2015, **13**, 500–508, DOI: **10.1016/j.nanoen.2015.03.018**.

18 W. Wang, *et al.*, Flexible Supercapacitors Based on Stretchable Conducting Polymer Electrodes, *Polymers*, 2023, **15**(8), 1856, DOI: **10.3390/polym15081856**.

19 R. Kumar, K. M. Johnson, N. X. Williams and V. Subramanian, Scaling Printable Zn–Ag $_2$ O Batteries for Integrated Electronics, *Adv. Energy Mater.*, 2019, **9**(13), 1803645, DOI: **10.1002/aenm.201803645**.

20 L. Yin, *et al.*, High Performance Printed AgO-Zn Rechargeable Battery for Flexible Electronics, *Joule*, 2021, **5**(1), 228–248, DOI: **10.1016/j.joule.2020.11.008**.

21 D. B. Ahn, S.-S. Lee, K.-H. Lee, J.-H. Kim, J.-W. Lee and S.-Y. Lee, Form factor-free, printed power sources, *Energy Storage Mater.*, 2020, **29**, 92–112, DOI: **10.1016/j.ensm.2020.04.007**.

22 A. Panagiotopoulos, *et al.*, 3D printed inks of two-dimensional semimetallic MoS $_2$/TiS $_2$ nanosheets for conductive-additive-free symmetric supercapacitors, *J. Mater. Chem. A*, 2023, **11**(30), 16190–16200, DOI: **10.1039/D3TA02508J**.

23 K.-C. Huang, *et al.*, Laser printer patterned sacrificed layer for arbitrary design and scalable fabrication of the all-solid-state interdigitated in-planar hydrous ruthenium oxide flexible micro supercapacitors, *J. Power Sources*, 2019, **417**, 108–116, DOI: **10.1016/j.jpowsour.2019.02.016**.

24 J.-H. Sung, S.-J. Kim, S.-H. Jeong, E.-H. Kim and K.-H. Lee, Flexible micro-supercapacitors, *J. Power Sources*, 2006, **162**(2), 1467–1470, DOI: **10.1016/j.jpowsour.2006.07.073**.

25 J.-K. Chih, A. Jamaluddin, F. Chen, J.-K. Chang and C.-Y. Su, High energy density of all-screen-printable solid-state microsupercapacitors integrated by graphene/CNTs as hierarchical electrodes, *J. Mater. Chem. A*, 2019, **7**(20), 12779–12789, DOI: **10.1039/C9TA01460H**.

26 A. Vyas, *et al.*, Impact of electrode geometry and thickness on planar on-chip microsupercapacitors, *RSC Adv.*, 2020, **10**(52), 31435–31441, DOI: **10.1039/D0RA05488G**.

27 J. Yoo, S. Byun, C.-W. Lee, C.-Y. Yoo and J. Yu, Precisely Geometry Controlled Microsupercapacitors for Ultrahigh Areal Capacitance, Volumetric Capacitance, and Energy

This journal is © The Royal Society of Chemistry 2024

J. Mater. Chem. A, 2024, **12**, 10229–10241 | **10239**

Density, *Chem. Mater.*, 2018, **30**(12), 3979–3990, DOI: **10.1021/acs.chemmater.7b03786**.

28 D. Pech, M. Brunet, T. M. Dinh, K. Armstrong, J. Gaudet and D. Guay, Influence of the configuration in planar interdigitated electrochemical micro-capacitors, *J. Power Sources*, 2013, **230**, 230–235, DOI: **10.1016/j.jpowsour.2012.12.039**.

29 A. Toor, A. Wen, F. Maksimovic, A. M. Gaikwad, K. S. J. Pister and A. C. Arias, Stencil-printed Lithium-ion micro batteries for IoT applications, *Nano Energy*, 2021, **82**, 105666, DOI: **10.1016/j.nanoen.2020.105666**.

30 J. Li, *et al.*, Scalable Fabrication and Integration of Graphene Microsupercapacitors through Full Inkjet Printing, *ACS Nano*, 2017, **11**(8), 8249–8256, DOI: **10.1021/acsnano.7b03354**.

31 A. Hodaei and V. Subramanian, Additive fabrication of fully-integrated high-performance millimeter-scale microsupercapacitors: Fine-tuning chemistry to maximize performance, *J. Power Sources*, 2023, **588**, 233738, DOI: **10.1016/j.jpowsour.2023.233738**.

32 H. Li and J. Liang, Recent Development of Printed Micro-Supercapacitors: Printable Materials, Printing Technologies, and Perspectives, *Adv. Mater.*, 2020, **32**(3), 1805864, DOI: **10.1002/adma.201805864**.

33 J. Park, Y. S. Kim, S. J. Sung, T. Kim and C. R. Park, Highly dispersible edge-selectively oxidized graphene with improved electrical performance, *Nanoscale*, 2017, **9**(4), 1699–1708, DOI: **10.1039/C6NR05902C**.

34 X. Wang, H. Bai and G. Shi, Size Fractionation of Graphene Oxide Sheets by pH-Assisted Selective Sedimentation, *J. Am. Chem. Soc.*, 2011, **133**(16), 6338–6342, DOI: **10.1021/ja200218y**.

35 X. Hao, *et al.*, Surfactant-mediated morphology evolution and self-assembly of cerium oxide nanocrystals for catalytic and supercapacitor applications, *Nanoscale*, 2021, **13**(23), 10393–10401, DOI: **10.1039/D1NR01746B**.

36 N. Maheswari and G. Muralidharan, Supercapacitor Behavior of Cerium Oxide Nanoparticles in Neutral Aqueous Electrolytes, *Energy Fuels*, 2015, **29**(12), 8246–8253, DOI: **10.1021/acs.energyfuels.5b02144**.

37 M. E. Khan, M. M. Khan and M. H. Cho, Ce3+-ion, Surface Oxygen Vacancy, and Visible Light-induced Photocatalytic Dye Degradation and Photocapacitive Performance of CeO2-Graphene Nanostructures, *Sci. Rep.*, 2017, **7**(1), 5928, DOI: **10.1038/s41598-017-06139-6**.

38 A. S. Dezfuli, M. R. Ganjali, H. R. Naderi and P. Norouzi, A high performance supercapacitor based on a ceria/graphene nanocomposite synthesized by a facile sonochemical method, *RSC Adv.*, 2015, **5**(57), 46050–46058, DOI: **10.1039/C5RA02957K**.

39 S. Tagliaferri, A. Panagiotopoulos and C. Mattevi, Direct ink writing of energy materials, *Mater. Adv.*, 2021, (2), 540–563, DOI: **10.1039/D0MA00753F**.

40 X. Lin, *et al.*, Screen-printed water-based conductive ink on stretchable fabric for wearable micro-supercapacitor, *Mater. Today Chem.*, 2023, **30**, 101529, DOI: **10.1016/j.mtchem.2023.101529**.

41 Y. Wang, Y.-Z. Zhang, D. Dubbink and J. E. Ten Elshof, Inkjet printing of δ-MnO2 nanosheets for flexible solid-state micro-supercapacitor, *Nano Energy*, 2018, **49**, 481–488, DOI: **10.1016/j.nanoen.2018.05.002**.

42 K. Shen, J. Ding and S. Yang, 3D Printing Quasi-Solid-State Asymmetric Micro-Supercapacitors with Ultrahigh Areal Energy Density, *Adv. Energy Mater.*, 2018, **8**(20), 1800408, DOI: **10.1002/aenm.201800408**.

43 K. Tang, *et al.*, 3D printed hybrid-dimensional electrodes for flexible micro-supercapacitors with superior electrochemical behaviours, *Virtual Phys. Prototyping*, 2020, **15**(1), 511–519, DOI: **10.1080/17452759.2020.1842619**.

44 W. Liu, *et al.*, Rapid Continuous Multimaterial Extrusion Bioprinting, *Adv. Mater.*, 2017, **29**(3), 1604630, DOI: **10.1002/adma.201604630**.

45 A. K. Miri, *et al.*, Microfluidics-Enabled Multimaterial Maskless Stereolithographic Bioprinting, *Adv. Mater.*, 2018, **30**(27), 1800242, DOI: **10.1002/adma.201800242**.

46 P. Cabanach, *et al.*, Zwitterionic 3D-Printed Non-Immunogenic Stealth Microrobots, *Adv. Mater.*, 2020, **32**(42), 2003013, DOI: **10.1002/adma.202003013**.

47 L. Ouyang, C. B. Highley, W. Sun and J. A. Burdick, A Generalizable Strategy for the 3D Bioprinting of Hydrogels from Nonviscous Photo-crosslinkable Inks, *Adv. Mater.*, 2017, **29**(8), 1604983, DOI: **10.1002/adma.201604983**.

48 A. A. Szklanny, *et al.*, 3D Bioprinting of Engineered Tissue Flaps with Hierarchical Vessel Networks (VesselNet) for Direct Host-To-Implant Perfusion, *Adv. Mater.*, 2021, **33**(42), 2102661, DOI: **10.1002/adma.202102661**.

49 Y. Fang, *et al.*, 3D Printing of Cell-Laden Microgel-Based Biphasic Bioink with Heterogeneous Microenvironment for Biomedical Applications, *Adv. Funct. Mater.*, 2022, **32**(13), 2109810, DOI: **10.1002/adfm.202109810**.

50 F. Qiu, *et al.*, An Ecofriendly Gel Polymer Electrolyte Based on Natural Lignocellulose with Ultrahigh Electrolyte Uptake and Excellent Ionic Conductivity for Alkaline Supercapacitors, *ACS Appl. Energy Mater.*, 2019, **2**(8), 6031–6042, DOI: **10.1021/acsaem.9b01150**.

51 N. Fazeli, E. Arefian, S. Irani, A. Ardeshirylajimi and E. Seyedjafari, 3D-Printed PCL Scaffolds Coated with Nanobioceramics Enhance Osteogenic Differentiation of Stem Cells, *ACS Omega*, 2021, **6**(51), 35284–35296, DOI: **10.1021/acsomega.1c04015**.

52 B.-A. Mei, O. Munteshari, J. Lau, B. Dunn and L. Pilon, Physical Interpretations of Nyquist Plots for EDLC Electrodes and Devices, *J. Phys. Chem. C*, 2018, **122**(1), 194–206, DOI: **10.1021/acs.jpcc.7b10582**.

53 G. Cidonio, M. Glinka, J. I. Dawson and R. O. C. Oreffo, The cell in the ink: Improving biofabrication by printing stem cells for skeletal regenerative medicine, *Biomaterials*, 2019, **209**, 10–24, DOI: **10.1016/j.biomaterials.2019.04.009**.

54 K. Huang, *et al.*, Anisotropy of graphene scaffolds assembled by three-dimensional printing, *Carbon*, 2018, **130**, 1–10, DOI: **10.1016/j.carbon.2017.12.120**.

55 M. Zhang, *et al.*, Spontaneous Alignment of Graphene Oxide in Hydrogel during 3D Printing for Multistimuli-Responsive

10240 | *J. Mater. Chem. A*, 2024, **12**, 10229–10241

This journal is © The Royal Society of Chemistry 2024

Actuation, *Adv. Sci.*, 2020, **7**(6), 1903048, DOI: **10.1002/advs.201903048**.

56 B. Zhou, *et al.*, Controlling surface porosity of graphene-based printed aerogels, *npj 2D Mater. Appl.*, 2022, **6**(1), 34, DOI: **10.1038/s41699-022-00312-w**.

57 J. Zhou, *et al.*, Ultrahigh volumetric capacitance and cyclic stability of fluorine and nitrogen co-doped carbon microspheres, *Nat. Commun.*, 2015, **6**(1), 8503, DOI: **10.1038/ncomms9503**.

58 X. Chen, *et al.*, Direct exfoliation of the anode graphite of used Li-ion batteries into few-layer graphene sheets: a green and high yield route to high-quality graphene preparation, *J. Mater. Chem. A*, 2017, **5**(12), 5880–5885, DOI: **10.1039/C7TA00459A**.

59 M. Mazloum-Ardakani, H. Mohammadian-Sarcheshmeh, H. Naderi, F. Farbod and F. Sabaghian, Fabrication of a high-performance hybrid supercapacitor using a modified graphene aerogel/cerium oxide nanoparticle composite, *J. Energy Storage*, 2019, **26**, 100998, DOI: **10.1016/j.est.2019.100998**.

60 L. Liu, *et al.*, All-Printed Solid-State Microsupercapacitors Derived from Self-Template Synthesis of Ag@PPy Nanocomposites, *Adv. Mater. Technol.*, 2018, **3**(1), 1700206, DOI: **10.1002/admt.201700206**.

61 S. Abdolhosseinzadeh, R. Schneider, A. Verma, J. Heier, F. Nüesch and C. (John) Zhang, Turning Trash into Treasure: Additive Free MXene Sediment Inks for Screen-Printed Micro-Supercapacitors, *Adv. Mater.*, 2020, **32**(17), 2000716, DOI: **10.1002/adma.202000716**.

62 C. Zhang, *et al.*, Additive-free MXene inks and direct printing of micro-supercapacitors, *Nat. Commun.*, 2019, **10**(1), 1795, DOI: **10.1038/s41467-019-09398-1**.

63 X. Tang, *et al.*, Generalized 3D Printing of Graphene-Based Mixed-Dimensional Hybrid Aerogels, *ACS Nano*, 2018, **12**(4), 3502–3511, DOI: **10.1021/acsnano.8b00304**.

64 E. Paparazzo, Use and mis-use of x-ray photoemission spectroscopy Ce3d spectra of Ce_2O_3 and CeO_2, *J. Phys.: Condens. Matter*, 2018, **30**(34), 343003, DOI: **10.1088/1361-648X/aad248**.

This journal is © The Royal Society of Chemistry 2024

J. Mater. Chem. A, 2024, **12**, 10229–10241 | **10241**